applied optics

Designing miniature x-ray optics for the SmallSat lunar science mission concept *CubeX*

Vinay L. Kashyap,[1,*] Jaesub Hong,[1] Suzanne Romaine,[1] Leandra Sethares,[1] Vincenzo Cotroneo,[1,2] Daniele Spiga,[2] and Larry Nittler[3]

[1]Center for Astrophysics | Harvard & Smithsonian, 60 Garden St, Cambridge, Massachusetts 02138, USA
[2]Osservatorio Astronomico di Brera, via Bianchi 46, Merate, LC, 23807, Italy
[3]Carnegie Institution, 5241 Broad Branch Rd NW, Washington, DC 20015, USA
*Corresponding author: vkashyap@cfa.harvard.edu

Received 26 March 2020; revised 18 May 2020; accepted 20 May 2020; posted 20 May 2020 (Doc. ID 393554); published 17 June 2020

Planetary remote-sensing instruments are often required to cover a relatively large field of view, ideally with a uniform angular resolution over the field, due to relatively large apparent sizes of planetary targets at close proximities. They also have to comply with relatively tight mass and volume constraints. For these reasons, planetary x-ray telescopes in the past were mainly collimation-based x-ray spectrometers without focusing optics. Recent advances in x-ray optics technology now enable compact focusing x-ray telescopes suitable for planetary science (e.g., *BepiColombo*). We present two design options for compact Wolter-I x-ray optics for a SmallSat lunar mission concept—the CubeSat X-ray telescope (*CubeX*). The primary objectives of *CubeX* are to map surface elemental abundances of selected lunar impact craters and to assess the feasibility of millisecond x-ray pulsar timing navigation in realistic deep space navigation environments. The Miniature X-ray Optics (MiXO) in *CubeX* utilizes electroformed NiCo alloy replication (ENR) technology, which provides many advantages over micro-pore optics (MPO) employed in *BepiColombo*. We carry out extensive ray traces over a grid of mirror parameters and explore a novel tapered shaped design of tightly nested shells, where both shell length and focal-plane offsets vary with shell diameter. One of the two configurations is optimized for large effective areas at low energies, while the other for lower mass and high-energy response. We compare their performances with those of conventional designs through the spatial resolution and effective area estimated by ray traces. © 2020 Optical Society of America

https://doi.org/10.1364/AO.393554

1. INTRODUCTION

X-ray observations of planetary bodies provide a powerful remote-sensing tool for determining elemental abundances, since x-ray fluorescence (XRF), induced either by solar x-ray flux or energetic ions, carries decisive signatures of elemental composition. These elements include major rock-forming components such as Mg, Al, Si, and Fe. Missions to carry out such observations have now become feasible due to the development of CubeSats and SmallSats. CubeSats are miniaturized space-going hardware typically put together in a few cubic units of 10 cm × 10 cm × 10 cm, while SmallSats are larger versions, typically occupying ∼100× the volume and with a mass <180 kg. Because of the smaller size and mass, they are cheaper to design, build, and launch, while allowing them to be optimized for highly specific science cases.

CubeX is a SmallSat lunar science mission selected for a concept study by the NASA Planetary Science Deep Space SmallSat Studies program in 2017 (Fig. 1). The x-ray imaging spectrometer (XIS), the main instrument of *CubeX*, is a compact, Wolter-I focusing x-ray telescope that identifies and spatially maps lunar crust and mantle materials excavated by impact craters [1,2]. The XIS obtains the elemental abundances of the target surface on the Moon through the measurements of fluorescent x-rays from the lunar surface triggered by solar x-rays. *CubeX* also serves as a pathfinder for autonomous precision deep-space navigation using x-ray pulsars (XNAV), where the precise time series from millisecond x-ray pulsars are used to calculate the trajectory of the spacecraft.

CubeX is designed to rideshare to the Moon as a secondary payload around the next solar maximum (2023–2027). After insertion into an elliptical orbit (∼500 × 5000 km), the *CubeX* spacecraft executes transfer maneuvers to reach a science optimized quasi-frozen high-altitude circular orbit at 6000 km, where *CubeX* will conduct 1 yr science operations.

The XIS on *CubeX* employs Miniature lightweight Wolter-I X-ray Optics (MiXO) and a novel combination of two high-spectral-resolution monolithic CMOS x-ray sensors and a high-timing-resolution silicon drift detector (SDD) to conduct both XRF measurements and XNAV demonstration without

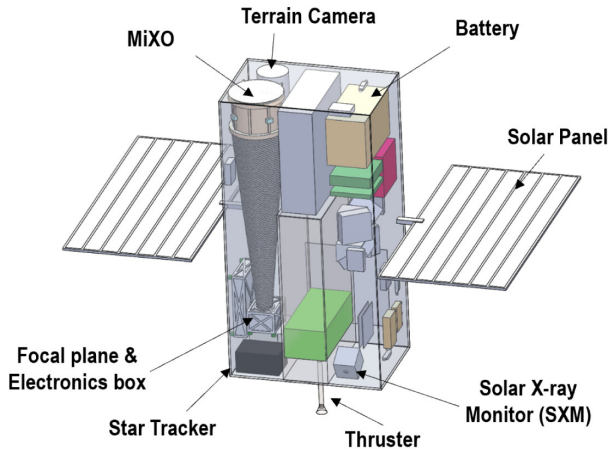

Fig. 1. *CubeX* spacecraft: *CubeX* is designed to be a secondary payload, weighing about 43 kg in a 35 × 23 × 68 cm volume. The x-ray imaging spectrometer (XIS) is at the front/left of the figure, spanning almost the full length of the configuration. The focal length of the baseline design of the XIS is 50 cm. See also Fig. 2 for a close-up of the x-ray mirror assembly of the Miniature X-ray Optics (MiXO) in the XIS.

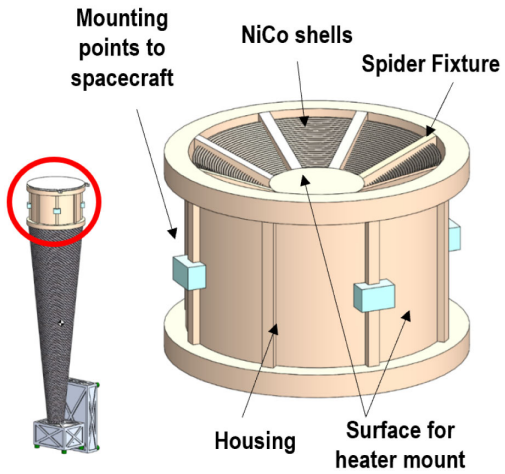

Fig. 2. Mirror module design of the MiXO for the *CubeX* XIS. The two configurations of nested shells we adopt are discussed in Section 3.

moving parts. MiXO for the XIS on *CubeX* is based on the electroformed nickel replication (ENR) [3,4]. The compact design of the MiXO enables miniaturization of Wolter-I x-ray telescopes and thus opens a door for a wide range of applications over multiple science disciplines including astrophysics, heliophyiscs, and planetary science.

In this paper, we illustrate our design approach for MiXO using *CubeX* as an example. To meet the unique instrumental requirements of *CubeX*, we present two design options for the MiXO of the *CubeX* XIS and compare their performances through Monte Carlo ray-tracing simulations. We introduce the MiXO of *CubeX* and the modeling tool in Section 2: the underlining technology (Section 2.A), the design requirements (Section 2.B), mirror nesting (Section 2.C), ray-tracing software (Section 2.D), and the tapered design (Section 2.E). The ray-trace results of the two adopted nested mirror structures are shown and compared in Section 3. We discuss the further enhancement work for the modeling and present an x-ray fluorescence map from simulated *CubeX* observations of a region around Picard Crater on the Moon in Section 4.

2. X-RAY MIRROR DESIGN

A. Wolter-I Optics

Most of modern x-ray astronomy missions have been designed around grazing-incidence optics with Wolter-I geometries. The Wolter-I configuration combines reflections, first from a parabolic, then from a hyperbolic surface to reduce off-axis aberrations (over a single bounce system) for imaging. To increase the collecting area of these telescopes, several barrel-shaped mirrors of varying diameter can be nested one inside the other along the same optical axis (see Section 2.C). The majority of x-ray missions employ either Al foil, glass, or nickel as the telescope substrate material. High-resolution (<1 arcsec) mirrors in the Chandra X-ray Observatory [5] were made by direct grinding and polishing of glass ceramic (zerodur), whereas an ENR technique used in XMM- *Newton* (58 shells) [6] allows for increased collecting area by greatly decreasing the thickness of each mirror shell to ≈ 1 mm (instead of ≈ 20 mm). In ENR, the resolution is determined by the quality of the polished and figured mandrel, and by stresses introduced during the replication process. The current 10–15 arcsec limit of ENR is well within the requirement for many missions including *CubeX*.

The ENR technique provides a number of advantages for miniaturization of optics over other alternatives such as micro-pore optics (e.g., MIXS-T on *BepiColombo* [7]). For instance, a closed figure of revolution (compared to telescopes using segmented mirrors) offers maximum rigidity and strength (e.g., against vibrations), reducing the support mass. Each shell also provides a complete image (both the first and second bounce mirrors), greatly simplifying co-alignment. Electroforming is well suited for replicating multiple copies, ideal for modular design. The composition of coating layers can be optimized for each shell to improve the effective area (e.g. Ir + C < 8 keV, graded W/Si >8 keV). Furthermore, the ENR technology is scalable for larger and smaller optics.

B. Requirements and Constraints for the MIXO of the *Cube*X XIS

Table 1 summarizes the requirements and constraints for the MiXO of the *CubeX* XIS. To cover a >100 km region of the lunar surface at an altitude of >5000 km with ≳3 km spatial resolution, *CubeX* requires a >1 deg diameter field of view (FoV) with a <1.5 arcmin resolution. As a secondary payload, the XIS has to meet the mass and volume constraints of the SmallSat spacecraft, which in turn constrains the mass and volume available for the MiXO as specified in Table 1.

X-ray optics with polynomial curvature [8] or Wolter-Schwarzschild configurations [9,10] can be used to improve point spread functions (PSFs) in the arcsec scale over a large FoV. The improvement from these methods is limited to a few arcsec reduction in the resolution, which is suitable for high-resolution x-ray telescopes. In contrast, for missions such as *CubeX*, which have more moderate requirements on angular resolution (∼0.5−1.5 arcmin), a mild defocusing of the optics can be a

Table 1. Requirements and Constraints for the MiXO of the *CubeX* XIS

Parameters	Requirements
Field of view (FoV)	>1 degree diameter
Angular resolution	<1.5 arcmin over FoV
Effective area at 1 keV	$\gtrsim$ 20 cm^2 at on-axis $\gtrsim$ 10 cm^2 at 25 arcmin
Parameters	**Constraints**
Volume	~12−15 cm dia. ×15 cm length
Mass (optics + structure)	$\lesssim$ 2−3 kg

more efficient way to improve the off-axis angular resolution at the cost of small degradation for on-axis angular resolution. The offsets of each mirror shell of the regular hyperbolic-parabolic optic from the focal plane depends on the diameter of the shells and is chosen through ray-tracing simulations. In addition, varying shell lengths, depending on the shell diameter (aka, the tapered design), allows a wider FoV coverage compared to the conventional optics design of the identical length for all nested shells (Fig. 4).

C. Tightly Nested Shells

A driving requirement for x-ray optics is the effective area. To achieve high effective area, multiple mirror shells can be nested tightly, but with enough spacing to avoid self-collimation, at least on-axis, such that a shell on the inside does not obstruct the rays reflecting off the shell on the outside. While obstruction up to a certain off-axis angle can be completely avoided, we preferred to adopt a tighter nesting approach that guarantees anyway the desired FoV, with the additional advantage of some self-baffling against stray light [11]. D. Spiga [12] developed a recursive solution based on analytical formulae that describe the geometry of nested parabolic and hyperbolic mirror surfaces. His solution optimizes shell spacing based on the required FoV for a given focal length and shell length, i.e., generates mirror shell configurations that are as closely packed as possible. We have adopted this algorithm in our work here with diameter-dependent variable shell lengths. In all cases we discuss below, we assume that the shell thicknesses are 0.2 mm, the focal length is 70 cm, the shell material density is 8.9 gm cm^{-3}, and that the FoV is 33 arcmin in radius. We explore mirror designs using ray traces (see Section 2.D), where shell diameters range from 30–130 mm and lengths range from ≈ 70−130 mm. (These are the combined lengths of the parabolic and hyperbolic segments, which are assumed to be equal for a given shell.)

D. Monte Carlo Ray-Tracing Simulation Using IRT/SAORT

For ray-tracing simulation, we utilize the interactive data language (IDL)-based ray-tracing modeling software Interactive Ray-Tracing (IRT). The IRT was developed at the University of Colorado in the 1980s to assist the design/development/analysis of optical systems for use in the infrared, visible, ultraviolet, and x-ray bands. We have developed the IDL-based add-on package to the IRT, Smithsonian Astrophysical Observatory Ray Trace (SAORT), which simplifies the optics configuration interface and makes it possible to run several iterations of a series of ray-tracing simulations over multiple configurations [13]. The code also implements scattering via micro-roughness and figure errors as a function of photon wavelength and ray angle. In all cases, we assume a surface roughness of 5 Å rms, a correlation length of 10 Å for the roughness, and a ripple amplitude of up to 10^{-4} radians of scattering.

E. Shell Lengths and Focus Offsets

Among the several requirements on the mirror design, the FoV (66′ diameter for *CubeX*) determines how small the shell diameter can be for a given shell length. In addition, the design should achieve the following characteristics: (1) the half-power diameter (HPD) should be $\lesssim 1'$ even at large off-axis locations; (2) the variation in HPD with off-axis should be small; (3) the scattering, and consequently the fraction of the flux that falls outside a 1′ aperture, should be small; and (4) the effective area should be maximized, even at high energies. We have explored a comprehensive set of single–mirror-shell settings through ray traces in order to determine which combination of parameters is optimal. The ray traces range over shell diameters 30 mm $< D <$ 130 mm, shell lengths 72 mm $< L <$ 130 mm, focal-plane offsets -0.5 mm $< f_p < +1.9$ mm, energies 0.5 keV $< E <$ 6.5 keV, and off-axis angles $0' < \theta < 33'$.

Based on these ray traces (see Appendix A), we have devised a simple mirror arrangement for the shells such that the shell lengths L (both the parabolic and hyperbolic segments are assumed to have the same length) decrease, and the focal-plane offsets f_p increase, as the shell diameters D decrease. We note that the nested mirrors solution [12] strictly applies when the horizontal intersection planes between the hyperbolic and parabolic components of the shells are nonvarying, but the magnitude of f_p relative to both the shell diameters and the focal length is large, and the resulting design remains valid. We develop two versions of this tapered design for configurations that seek to trade off mirror size and weight against total effective area. We describe the performance of these configurations in Section 3 and demonstrate its trade-offs in Section 4 in comparison with conventional designs where the shell lengths are constant and no defocus is applied.

3. RESULTS

We consider two cases: one compact ($D \leq 105$ mm, $L \leq 80$ mm, $N_{\rm shell} = 34$) and one large ($D \leq 130$ mm, $L \leq 110$ mm, $N_{\rm shell} = 24$). In the compact case, the number of shells is bounded by the restriction of the required FoV, and the configuration occupies a smaller volume and has less mass (see Table 2). The larger configuration will have a larger effective area at low energies, but it will have larger volume and mass; furthermore, the number of shells is capped at 24, which limits the number of mandrels required for fabrication (since each shell requires a separate mandrel), leading to reduced overall cost, as well as schedule savings for assembly of the optics module. The trend in shell length with shell diameter is discussed in Appendix A, and we adopt a general 22% drop in shell length from the outside to the center. The adopted focal-plane

Table 2. *CubeX* Tapered Configurations: Compact versus Large

Parameters	Compact	Large
FoV diameter [arcmin]	66	
Focal length [mm]	500	
Shell thickness [mm]	0.2	
Shells	34	24
Max diameter [mm]	105	130
Min diameter [mm]	41.6	62.5
Geometric area [cm^2]	46	80
EA on axis at 1 keV [cm^2]	23.3	34.5
EA 20′ at 1 keV [cm^2]	14.7	23.5
EA 30′ at 1 keV [cm^2]	8.6	12.9
HPD on axis at 1 keV [arcsec]	28.1	29.4
HPD 20′ at 1 keV [arcsec]	26.8	28.4
HPD 30′ at 1 keV [arcsec]	52.1	50.0

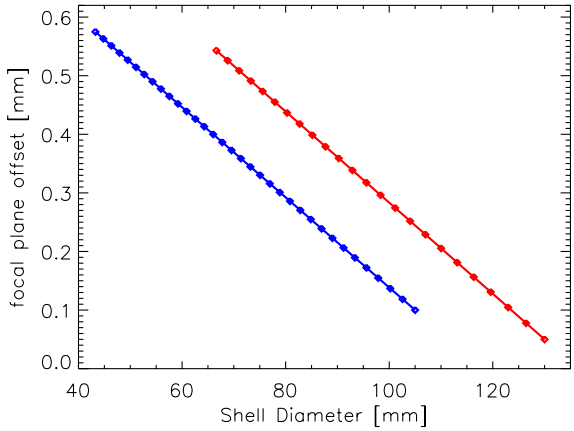

Fig. 3. Adopted variation in focal-plane offset for shells of a given diameter, for both the large (red) and compact (blue) designs. Diamonds represent the diameters of the shells in each configuration (see also Fig. 4).

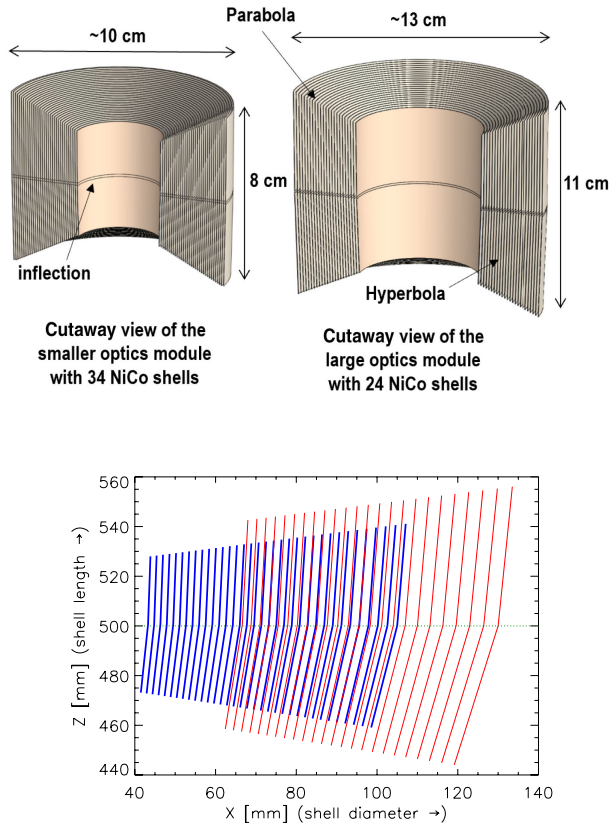

Fig. 4. Sketches of the *CubeX* tapered configurations drawn to scale. The cutaway views of the small (*top left*) and large (*top right*) configurations are also shown. The lower panel shows a line drawing cutouts of the profiles, with the large (red) and compact (blue) shells superposed. The horizontal dotted line indicates the focal length.

offsets are shown in Fig. 3. A diagram of the nested shells in the two cases is shown in Fig. 4.

The HPD as a function of off-axis angles is shown for both configurations in Fig. 5 for several photon energies. First, note that the HPD remains relatively flat out to ≈ 20 arcmin, and even though it increases with the off-axis angles afterwards, it remains below the 1.5 arcmin requirement (see Table 1), even at the edge of the FoV for most cases. The PSF also maintains a more or less uniform shape out to the edge of the FoV at 30 arcmin as shown in Fig. 6.

We compute the effective area (EA) as a combination of the geometric area, reflectivity, and aperture size effects. The geometric area is the projected area visible to a distant source. Various coating options will be explored to improve the high-energy response (e.g., multilayers like W/Si). Finally, we compute the fraction of the ray-trace photons from a point source that falls within a 0.5′ radius of the centroid and include this correction as part of the estimated EA. This factor corrects for the fact that photons that scatter much farther away are likely to be lost in the background and will not contribute to the detection of features. We show the EAs computed in this manner for several combinations of off-axis angles and photon energies in Figs. 7 and 8. In general, the MiXO designs chosen achieve the highest EA and the smallest HPD for on-axis sources at low energies; the EA drops with both off-axis angle and energy, with a sharp feature at the iridium edge at ≈ 2 keV. At low energies, the EA is mostly preserved at >40% levels at large off-axis angles, but at high energies (>3 keV) the on-axis EA is reduced by factors of 10, with off-axis EA dropping even faster. The compact design, with more and narrower-spaced shells preserves the high-energy EA better because of the higher reflectivity at smaller incidence angles with the IrC coating.

4. DISCUSSION

Both the compact and large tapered configurations meet the *CubeX* requirements. They enable <1 arcmin HPD over 1 deg diameter FoV up to ∼5 keV and achieve >20 cm^2 on-axis effective area and ≳10 cm^2 at 25–30 arcmin off-axis angles below 2 keV. The response for hard x-rays above 2 keV drops noticeably with the IrC coating, and more rapidly in the large optics configuration due to larger graze angles. We anticipate that improvements to enhance the hard x-ray response are possible with multilayer coatings. As long as the spacecraft volume is available, the large configuration has advantages in

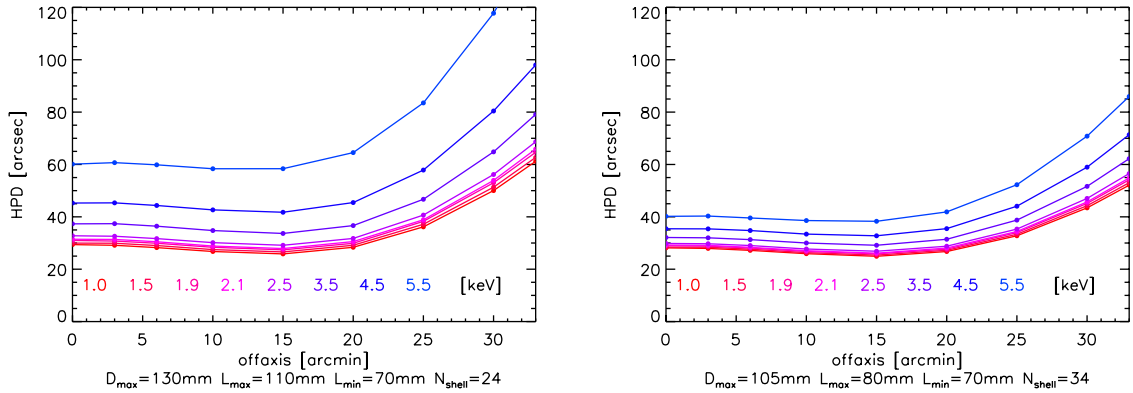

Fig. 5. Half-power diameter (HPD) as a function of off-axis location for the large (*left*) and small (*right*) designs. The different colored curves represent different photon energies ranging from 1 (red) to 5.5 keV (purple) as noted by the colors of the energy value labels along the bottom parts of the plots. See also Fig. 6 for images of the PSF.

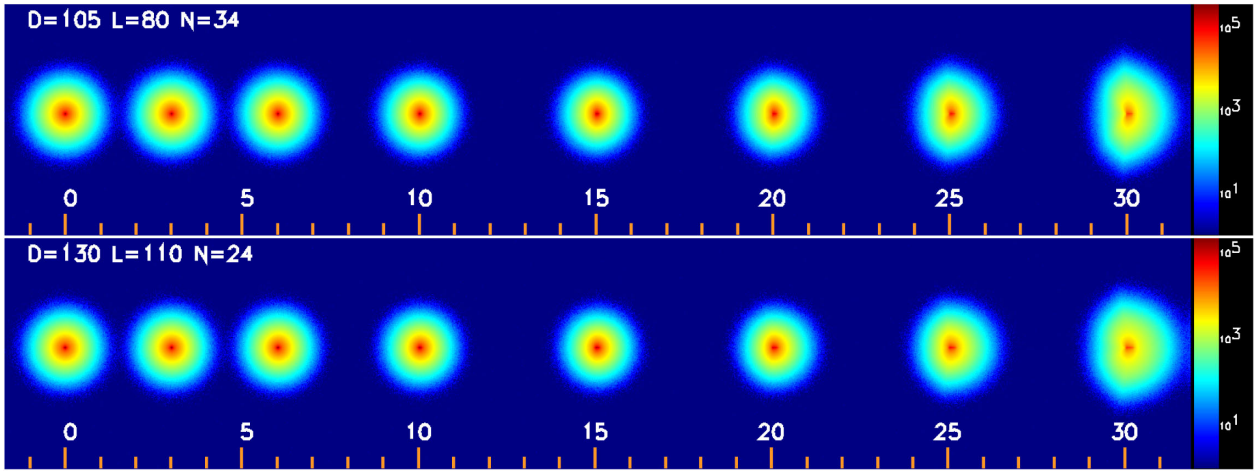

Fig. 6. Ray-traced images at various off-axis angles at 0′, 3′, 6′, 10′, 15′, 20′, 25′, 30′, for the compact (*top*) and large (*bottom*) configurations. The images combine monochromatic photons from several energies from 0.5–6.5 keV and are presented in a logarithmic intensity scale. The number of photons obtained at each energy is determined by the effective area. The tick marks are spaced 1 arcmin apart. The adopted mirror configurations keep image quality steady across a wide range of off-axis angles.

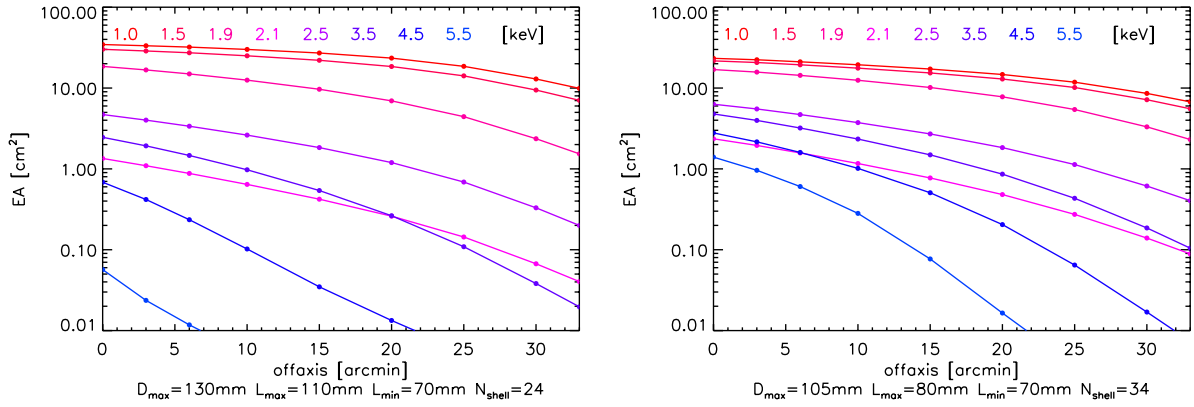

Fig. 7. Effective area (EA) as a function of off-axis location for the large (*left*) and small (*right*) designs. The different colored curves are for different photon energies as in Fig. 5. A different projection of the same information, EA versus energy for different off-axis angles is shown in Fig. 8.

terms of performance, a lower cost arising from smaller number of shells, and ease of construction due to larger spacing of the shells. If the mission allows, having multiple telescope modules is an attractive option for cost and schedule savings in optics fabrication and assembly while achieving high performance and redundancy.

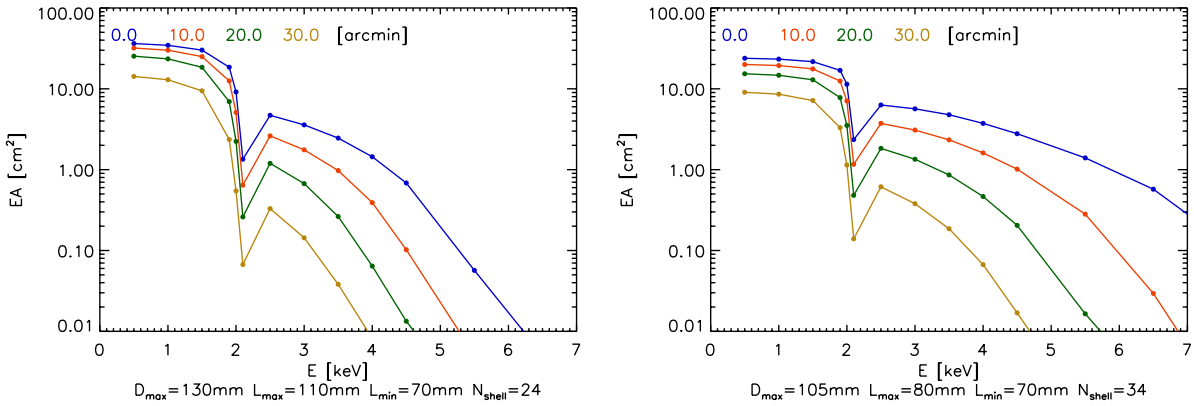

Fig. 8. EA as a function of energy for various off-axis locations (on-axis: blue; 10′: orange; 20′: green; 30′: yellow) for the large (*left*) and small (*right*) designs. This is a different projection of the information presented in Fig. 7.

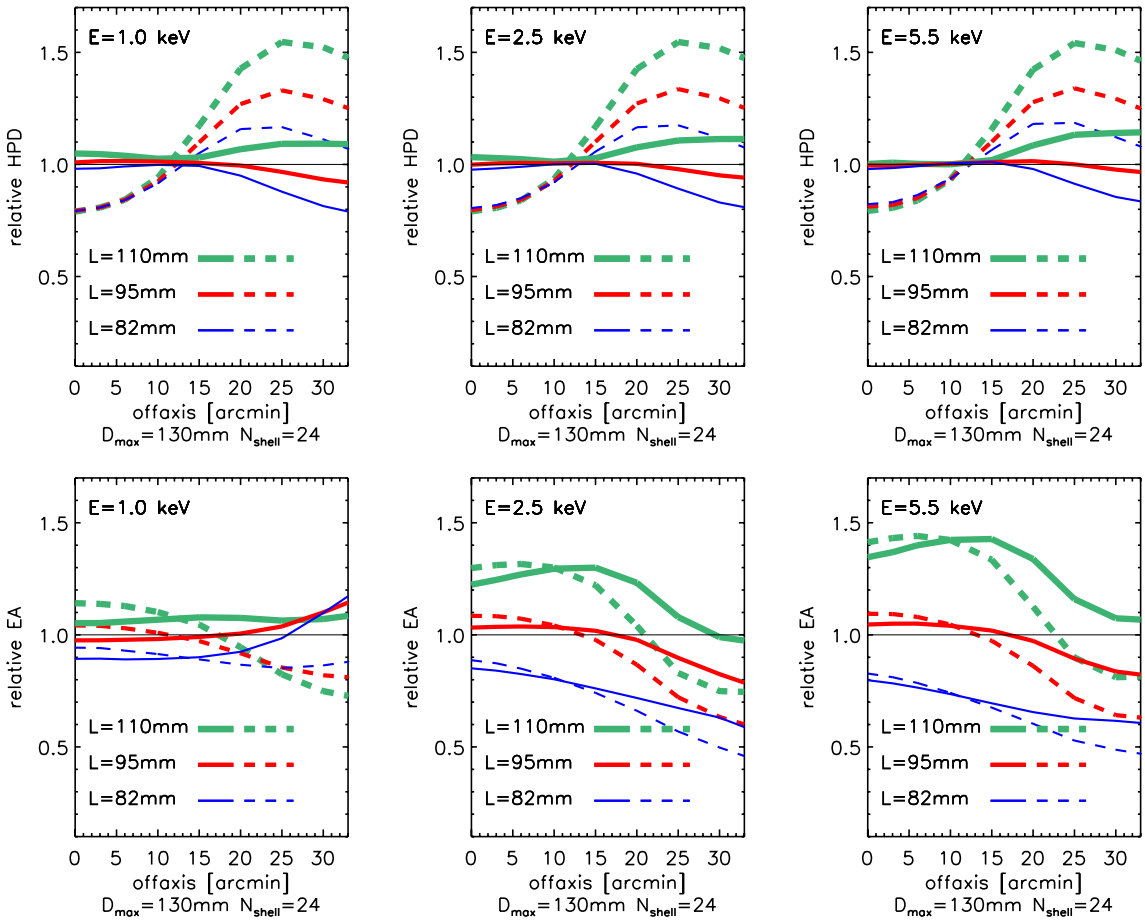

Fig. 9. Ratios of HPD and EA of conventional to large tapered ($D_{\max} = 130$ mm, $N_{\text{shell}} = 24$) designs for different combinations of photon energy, off-axis location, shell lengths, and focal-plane offsets. The ratios of the HPDs are shown in the *top panels*, and those of EA in the *bottom panels*, as functions of off-axis location. *Solid curves* correspond to the case where the conventional designs have $f_p = 0.3$ mm, corresponding to the average value of the focal-plane offsets of the large tapered configuration (see Fig. 3). *Dashed curves* correspond to the case where $f_p = 0$ mm, i.e., there is no defocusing. Several cases of conventional configurations of constant shell lengths L are shown, corresponding to the maximum ($L = 110$ mm; *thick green curves*), average ($L = 95$ mm; *normal red curves*), and minimum ($L = 82$ mm; *light blue curves*) of the range of L that comprises the large tapered configuration. Note that in all cases the outermost shell diameter is set at $D_{\max} = 130$ mm and the configurations have 24 shells. Different photon energies are represented in different columns, with low ($E = 1$ keV at *left*), medium ($E = 2.5$ keV in the *middle*), and high ($E = 5.5$ keV at *right*).

We also consider the question of how the tapered configurations compare against conventional designs where the shell lengths and focal-plane offsets are held constant. These conventional configurations are significantly easier to construct from an engineering standpoint. We show the differences in HPD and EA for several cases of conventional design relative to the large tapered configuration in Fig. 9. We compute the HPD and EA for three options of shell lengths 82, 95, and 110 mm (the shortest, the average, and the longest shell lengths of the large configuration, shown in blue, red, and green, respectively), combined with two options for fixed focal-plane offsets at 0 mm and 0.3 mm (i.e., no offset and an average of the offset shown in Fig. 3, displayed as dashed and solid lines, respectively). The conventional optics configurations without focal-plane offsets all show large degradation (up to 50%) in both HPD and EA at >15 arcmin off-axis angles, regardless of the chosen shell lengths. This indicates that on-axis defocusing is essential to achieve a uniform response over a large FoV, especially beyond 15 arcmin off-axis angles. Among the cases where a fixed 0.3 mm defocusing is used, as expected, the longer shell configurations have higher EAs and generally also larger HPDs. Among the conventional designs, the optics with the average constant shell length performs best, with the HPD being either approximately at the same level as in the tapered configuration or smaller (by a few percent) throughout the FoV. It also achieves a higher EA at low energies, but it drops by $>10\%$ at large off-axis angles (>20 arcmin) for higher energies. This is consistent with the behavior of the summarizing metric μ [Eq. (6); see Appendix A], which shows that tapered configurations are preferred for large off-axis and high energies. Similar results are obtained when constant shell length and constant defocus configurations are compared to the compact tapered configuration. We thus conclude that the tapered design provides useful trade-offs between HPD and EA over the large FoV and at high energies. Nevertheless, we note that the tapered design requires a larger encasing volume compared to the average shell length conventional design, and that a constant focal-plane offset may provide a more cost-effective approach to improving performace across the FoV.

A. Simulations of Lunar Observations

Figure 10 illustrates a simulated 500 ksec observation of a region around the lunar Picard crater with *CubeX* using the compact MiXO configuration. In this example, the composition of smaller craters is assumed to be consistent with lunar mare basalt and the rest with lunar anorthosite. The x-ray image is a composite of Fe-L in red, Mg-L in green, and Al-K lines in blue. We set the mare surfaces to be rich in Al, and the crater walls to be rich in Fe, with Mg spread out evenly. The expected map of fluorescent x-rays from the sunlit phase is then convolved with the energy- and off-axis angle-dependent PSF of *CubeX* for the photon energies at the three lines. The image shows surface structure in x-ray with unprecedented detail (1–3 km scales), demonstrating that surface composition changes can be clearly discerned.

B. Current Limitations and Future Enhancements

We have designed two configurations of compact Wolter Type-I optics to carry out imaging of lunar x-ray fluorescence at sub-arcmin spatial scales. We demonstrate via ray traces that the configurations meet the requirements. Several improvements to the ray-trace models are still possible to make further improvements or obtain better estimates. For instance, the ray traces currently do not account for changes in the reflectivity due to the changes in graze angle with azimuth at large off-axis positions; these (second-order) corrections are being included in SAORT and will be available shortly. Further, the effective area estimates do not include the effects of obscuration due to mirror support structures, which will likely reduce the effective areas by $\approx 10\%$. Note that we have conservatively assumed an iridium-carbon (IrC) coating for the mirrors to describe the reflectivity. This coating results in a large absorption edge at ≈ 1.9 keV and causes a large drop in the EA at higher energies. We are exploring multilayer coatings that are expected to improve the high-energy response. We also plan to explore the effects of shell misalignments through simulations, e.g., by imposing a random jitter on the shell locations during ray tracing.

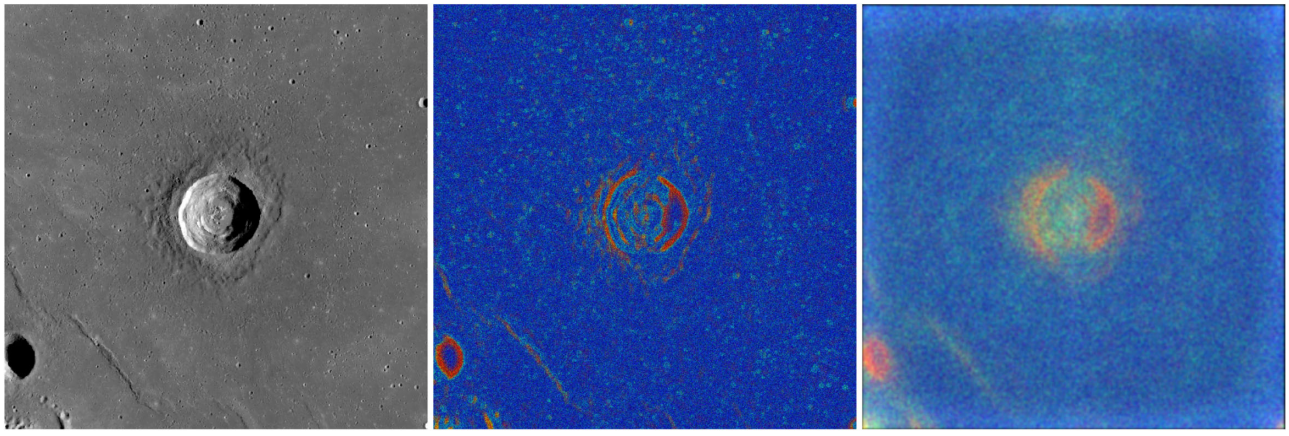

Fig. 10. Demonstrating the performance of *CubeX* with a ray trace of a 100 km wide region around Picard crater at the North-East of the Moon. (*Left*) An optical image taken with *Lunar Reconnaissance Orbiter* (LRO). (*Middle*) Mock-up of a nominal emission map of x-ray XRFs (see text). (*Right*) A ray trace of a 500 ksec observation of the region with *CubeX*. The x-ray ray-trace image is made with Fe-L (red), Mg-K (green), and Al-K (blue) lines. The composition of the region is assumed to be a varying composite of lunar mare basalt (higher Fe and Mg abundances) and anorthositic breccia meteorite (higher Al abundance). The composition variation at 1–3 km scales is easily detectable with the MiXO.

5. SUMMARY

We have explored the performance of compact Wolter-I x-ray optics module through the changes in the effective area and HPD from various shell spacings, mirror diameters, shell lengths, and focal-plane offsets. Requiring that the HPD is less than 1.5 arcmin throughout the FoV, and that the effective area for on-axis sources at low energies be $>20\ \mathrm{cm}^{-2}$, we have devised a novel tapered configuration where the inner shells are made progressively shorter with increasing offsets from the focal plane.

We have compared two specific realizations of this tapered design: a compact one with a maximum mirror diameter of 105 mm and with 34 shells, and a larger version where the maximum diameter is 130 mm but is limited to 24 shells. The former is advantageous when there is a severe volume constraint, and it has a better high-energy response than the latter, which, however, has a larger overall effective area at lower energies. The latter has significant advantages in the fabrication and assembly cost due to a smaller number of shells. The relatively larger shell spacing in the latter allows easier alignment during the assembly.

We have developed the mirror design configuration for the case of *CubeX*, but our design approach developed here is applicable to various CubeSat/SmallSat x-ray missions, tailored to their unique requirements. For instance, SmallSat Solar Axion & Activity X-ray Imager (*SSAXI*; [14]) requires about 40 arcmin diameter FoV and <1 arcmin resolution in the 0.5–5 keV band. High solar x-ray flux keeps the EA requirement relatively low ($<0.1-10\ \mathrm{cm}^2$, depending on the energy band). Therefore, to cover the wide dynamic range of the solar x-ray flux, depending on the energy range, the optics requirements for *SSAXI* can be met with multiple telescopes, each optimized for different energy bands (three types). Another example is SmallSat Exosphere Explorer of hot Jupiters (*SEEJ*; [15]), which requires 10 arcmin diameter FoV and 0.5 arcmin angular resolution in the 0.5–1.5 keV band. A main driving requirement for *SEEJ* is the high effective area ($\sim 100\ \mathrm{cm}^2$), which can be met by multiple modules of the identical small telescopes.

APPENDIX A: FIGURE OF MERIT

The constraints that drive the *CubeX* design are easily stated: a sharp PSF, with HPD $< 1'$; small variations in the HPD across the FoV; minimal loss due to scattering; and maximal effective area even at high energies. These constraints are also subject to the size and weight requirements of a CubeSat.

In order to simplify the design process, we codify the multiply-dimensioned constraints into a mathematically tractable scalar figure of merit μ that allows us to easily compare different configurations. This codification is guided by devising mathematical forms that mimic the constraints at the boundaries of their applicability. The metric is devised such that larger values are better than smaller values. We describe each component of this metric in detail below. There are several mirror parameters that control the quality of the mirror response. By examining the variations in μ, we gain a qualitative understanding of how the length and focal-plane offset should behave for different shells. We explore the variations in μ through ray traces. We consider single-shell mirrors with diameters $30\ \mathrm{mm} < D < 130\ \mathrm{mm}$, with shell lengths $72\ \mathrm{mm} < L < 128\ \mathrm{mm}$, with focal-plane offsets $-0.5\ \mathrm{mm} < f_p < +1.9\ \mathrm{mm}$, at several photon energies $0.5\ \mathrm{keV} < E < 6.5\ \mathrm{keV}$ for point sources located at ≈ 6000 km at off-axis angles $0' < \theta < 33'$. We show an illustrative set of plots in Fig. 11 that shows how μ varies with L and D for different instances of f_p, θ, and E.

(1) Sharp PSF: The PSF is required to have HPD < 1 arcmin at all locations in the FoV. However, to allow for potential error budgets, we prefer to aim for a smaller value and to strongly deprecate ray traces that generate HPD > 45″. We achieve this by weighting the ray traces with a Gaussian weighting function that reaches its 1σ extension at HPD = 45″. Specifically, we adopt a weighting function $N(\mathrm{HPD};\ \mathrm{mean} = 25'',\ \mathrm{variance} = 20''^2)$. However, note that such a profile also deprecates ray traces with small values of HPD, which is counter-productive. We deem all PSFs that have HPD < 40″ to be equally acceptable and thus replace the Gaussian weighting with a flat weighting. Thus, the figure of merit that describes the sharpness of a PSF produced in a given ray trace is

$$\mu_{\mathrm{sharp}} = 1 \quad \text{for HPD} < 40'', \tag{1}$$

$$\mu_{\mathrm{sharp}} = C_{\mathrm{sharp}} \cdot e^{-\frac{(\mathrm{HPD}-25'')^2}{2(20'')^2}} \quad \text{for HPD} \geq 40'', \tag{2}$$

where $C_{\mathrm{sharp}} = 1.325$ is the normalization factor to ensure continuity in μ_{sharp} across HPD = 40″.

(2) Consistent imaging across FoV: A desirable feature of an imaging instrument is that the HPD does not vary by a large amount over the FoV. To ensure this, we compute the ratio of the HPDs at the aimpoint to that near the edge of the FoV and use this ratio as the weighting factor for the corresponding ray trace. For any ray traces that have the off-axis HPD being smaller than the on-axis HPD, we cap the ratio at unity. That is, we define

$$\mu_{\mathrm{flat}} = \min\left\{\frac{\mathrm{HPD}(\theta = 0')}{\mathrm{HPD}(\theta = 30')}, 1\right\}, \tag{3}$$

to preferentially weight those mirror shell settings where the off-axis HPD degrades less.

(3) Minimize scattering: In addition to the core of the PSF being sharp (encapsulated by the HPD), it is advantageous to also minimize scattering out of the aperture. Such scattering reduces the counts observed in the core (and hence decreases the effective area) as well as contributes to a diffuse background that reduces detectability of weak features. We keep track of this by computing the fraction of the events that make it to the focal plane that are included inside a circle of diameter 1′. The smaller this number, the more events are scattered out; it thus forms a natural weight to the shell settings:

$$\mu_{\mathrm{aperture}} = f_{\mathrm{aperture}}. \tag{4}$$

(4) Maximize effective area: Finally, we want to have the largest effective areas that are possible at all energies. The largest factor that determines this is the exposed area of the mirror shell and is thus proportional to D^2. In addition, the incident angle has a significant effect on the effective area at energies $E > 2$ keV, such that shells with smaller diameters will have larger effective areas than those with larger diameters at small off-axis angles. We thus adopt the ratio of the effective area

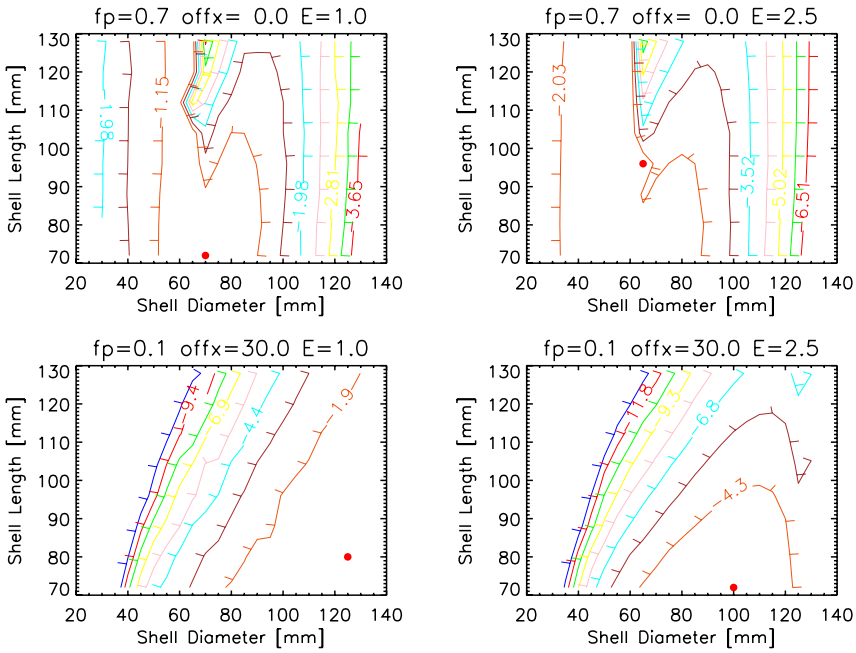

Fig. 11. Contour plots showing the dependence of the metric $\log(\mu)$ [see Eq. (6)] with shell length and diameter for several exemplary focal-plane offsets, off-axis positions, and photon energies. The dashed line represents the adopted variation in shell length with shell diameter; inner shells are chosen to be shorter as constant or increasing shell lengths lead to solutions with small μ for large f_p and large θ. The red dots show the locations of the maximum in μ for that slice. The adopted trend in shell length is not designed to be an optimal fit to μ but merely encodes a simplified design that follows the trends visible in the ray traces.

divided by the maximum effective area in the entire ray trace set as the weight factor

$$\mu_{\mathrm{EA}} = \frac{A_{\mathrm{eff}}(D,\, L,\, f_p,\, E,\, \theta)}{\max(A_{\mathrm{eff}})}. \tag{5}$$

The overall metric is then the product of all four components:

$$\mu = \mu_{\mathrm{flat}} \cdot \mu_{\mathrm{sharp}} \cdot \mu_{\mathrm{aperture}} \cdot \mu_{\mathrm{EA}}. \tag{6}$$

We explore the behavior of various single-shell configurations and use μ to summarize how changing the shell diameter D, shell length L, focal-plane offset f_p, off-axis angle θ, and photon energy E affect the quality of the mirrors. In Fig. 11, we show some examples of how the metric depends on D and L for several instances of f_p (small, 0.1 mm; and large, 0.7 mm), θ (on-axis and far off-axis), and E (1 and 2.5 keV). For small θ and large f_p, μ tends to be flat along L for a given D, but it decreases for both small and large D. Larger E tends to tilt the ridges such that large L are not favorable. As θ increases, larger D become favorable, and the surfaces are better behaved for smaller f_p. Based on such considerations, we develop the tapered design described in Section 2.E, where L decreases with D and each shell is defocused by different amounts.

Funding. National Aeronautics and Space Administration (NAS8-03060, NNX16AL75G, NNX17AK29G).

Disclosures. The authors declare no conflicts of interest.

REFERENCES

1. J. Hong, S. Romaine, L. Nittler, D. Kring, N. Petro, K. Gendreau, J. Mitchell, L. Winternitz, R. Kraft, A. Kenter, G. Prigozhin, R. Masterson, J. Evans, K. Bonner, A. Clark, A. Dave, A. Dono-Perez, M. Ebert, A. Kashani, D. Larrabee, D. Mauro, S. Montez, J. Mueting, D. Nguyen, L. Plice, K. Ronzano, L. Shen, T. Snyder, J. Stupl, and B. Wickizer, "CubeSat x-ray telescope (CubeX) for lunar elemental abundance mapping and millisecond X-ray pulsar navigation," in *Lunar and Planetary Science Conference* (2018), p. 2793.
2. J. Stupl, M. Ebert, and J. Hong, and CubeX Team, "CubeX: a compact x-ray telescope enables both x-ray fluorescence imaging spectroscopy and pulsar timing based navigation," in *32nd Annual AIAA/USU Conference on Small Satellites*, Logan UT, 4–9 August, (NASA, 2018), pp. SSC18-V-05.
3. O. Citterio, P. Conconi, M. Ghigo, F. Mazzoleni, G. Pareschi, and L. Peverini, "Development of soft and hard x-ray optics for astronomy," Proc. SPIE **4138**, 43–57 (2000).
4. B. D. Ramsey, "The development of focusing optics for the hard-x-ray region," Adv. Space Res. **38**, 2985–2988 (2006).
5. M. C. Weisskopf, "The Chandra X-ray Observatory: an overview," Adv. Space Res. **32**, 2005–2011 (2003).
6. F. Jansen, D. Lumb, B. Altieri, J. Clavel, M. Ehle, C. Erd, C. Gabriel, M. Guainazzi, P. Gondoin, R. Much, and R. Munoz, "XMM-Newton Observatory-i. The spacecraft and operations," Astron. Astrophys. **365**, L1–L6 (2001).
7. G. W. Fraser, J. D. Carpenter, D. A. Rothery, J. F. Pearson, A. Martindale, J. Huovelin, J. Treis, M. Anand, M. Anttila, M. Ashcroft, and J. Benkoff, "The mercury imaging x-ray spectrometer (MIXS) on BepiColombo," Planet. Space Sci. **58**, 79–95 (2010).
8. C. J. Burrows, R. Burg, and R. Giacconi, "Optimal grazing incidence optics and its application to wide-field x-ray imaging," Astrophys. J. **392**, 760–765 (1992).
9. L. P. van Speybroeck and R. C. Chase, "Wolter-Schwarzchild telescopes for x-ray astronomy," Appl. Opt. **12**, 1042–1044 (1973).
10. L. P. van Speybroeck and R. C. Chase, "Design parameters of paraboloid-hyperboloid telescopes for x-ray astronomy," Appl. Opt. **11**, 440–445 (1972).

11. D. Spiga, "Analytical computation of stray light in nested mirror modules for x-ray telescopes," Proc. SPIE **9603**, 107–124 (2015).
12. D. Spiga, "X-ray mirror module analytical design from field of view requirement and stray light tolerances," Proc. SPIE **9905**, 99056R (2016).
13. L. Sethares, V. Cotroneo, J. Hong, V. Kashyap, and S. Romaine, "Evaluating the projected performance of Wolter-I x-ray telescope designs for SmallSats," Proc. SPIE **11119**, 111191Q (2019).
14. J. Hong, S. Romaine, A. Kenter, C. Moore, K. Reeves, B. Ramsey, K. Kilaru, J. K. Vogel, J. R. Armendariz, H. H. Hudson, and K. Perez, "SmallSat solar axion and activity x-ray imager (SSAXI)," Proc. SPIE **11118**, 297–308 (2019).
15. S. J. Wolk, J. Hong, S. Romaine, K. Poppenhaeger, A. Kenter, A. V. Moorhead, D. L. Gallagher, C. S. Moore, M. Elvis, R. Kraft, J. Drake, V. Kashyap, E. Winston, B. Wargelin, I. Pillitteri, D. Jerius, M. Stahl, B. Wiegmann, and C. Loghry, "SEEJ: SmallSat Exosphere Explorer of hot Jupiters," Proc. SPIE **11118**, 89–104 (2019).